

RSC Advances



This is an *Accepted Manuscript*, which has been through the Royal Society of Chemistry peer review process and has been accepted for publication.

Accepted Manuscripts are published online shortly after acceptance, before technical editing, formatting and proof reading. Using this free service, authors can make their results available to the community, in citable form, before we publish the edited article. This *Accepted Manuscript* will be replaced by the edited, formatted and paginated article as soon as this is available.

You can find more information about *Accepted Manuscripts* in the [Information for Authors](#).

Please note that technical editing may introduce minor changes to the text and/or graphics, which may alter content. The journal's standard [Terms & Conditions](#) and the [Ethical guidelines](#) still apply. In no event shall the Royal Society of Chemistry be held responsible for any errors or omissions in this *Accepted Manuscript* or any consequences arising from the use of any information it contains.

Enhanced Thermoelectric Properties in Pb-doped BiCuSeO Oxyselenides Prepared by Ultrafast Synthesis

Guang-Kun Ren,^a Jin-le Lan,^b Sajid Butt,^{a,c} Kyle J. Ventura,^a Yuan-Hua Lin,^{a*} Ce-Wen Nan^a

^a State Key Laboratory of New Ceramics and Fine Processing, Tsinghua University, Beijing 100084, P. R. China

^b College of Materials Science and Engineering, Beijing University of Chemical Technology, Beijing 100083, P. R. China

^c Department of Materials Science and Engineering, Institute of Space Technology, Islamabad 44000, Pakistan

Abstract

BiCuSeO oxyselenides have been successfully fabricated by self-propagating high-temperature synthesis (SHS). Compared with the SHS process of the binary or ternary alloys, thermal analysis indicates the ignition temperature of quaternary layered BiCuSeO oxyselenides approaches the second lower melting point of the compound. The ZT value of SHS-synthesized BiCuSeO is almost 1.5 times larger than that of the solid state reaction (SSR) product at 873K. This is attributed to the existing amorphous region, nano-pores, and optimized grain size. Furthermore, with the partial substitution of Pb^{2+} for Bi^{3+} , ZT was enhanced through the optimization of charge carrier concentration and band gap narrowing. This achieved a ZT of 0.91 at 873K for $Bi_{1-x}Pb_xCuSeO$ ($x=0.04$). Combining with the Debye-Callaway model

analysis, the ultralow lattice thermal conductivity of BiCuSeO can potentially be derived from the synergistic effect of intrinsic point defects, efficient grain boundaries and some other mechanisms.

Introduction

Today's increasing energy demands require not only new energy sources but also utilization of traditional energy sources more efficiently by minimizing energy losses. Thermoelectric devices are a key-technology for harvesting the waste heat from energy production processes, and turning it into usable electricity. These devices do this without any moving parts, and are completely scalable.¹ The conversion efficiency of such thermoelectric devices is evaluated by a dimensionless figure of merit $ZT=S^2\sigma T/\kappa_t$, where, S is the Seebeck coefficient, σ the electrical conductivity, κ_t the total thermal conductivity and T the absolute temperature. At present, all the available thermoelectric devices must confront either the problem of low conversion efficiency and/or thermal and chemical instability at high temperature.^{2,3} These challenges require the discovery of new thermoelectric materials with higher efficiency and/or the novel synthesis methods for the optimization of transport properties in the existing thermoelectric materials.⁴⁻⁸

In a broader view, thermoelectric materials can be divided into two categories: metallic alloys and oxide-based compounds. Most of the alloy-based materials exhibit higher ZT values; typical examples are Bi_2Te_3 ,⁹ PbTe ,¹⁰ SiGe ¹¹ and some other systems like half-Heusler¹² and skutterudites.¹³ Despite their high ZT values, expensive elements, phase-transitions, toxicity and thermal instability at high temperature, make these materials difficult to apply. In order to solve or minimize these issues, oxide-based materials including layered compounds such as $\text{Ca}_3\text{Co}_4\text{O}_9$ ¹⁴

and NaCoO₂,¹⁵ perovskite-like compounds like CaMnO₃¹⁶ and SrTiO₃,¹⁷ and simple oxides like ZnO¹⁸ and In₂O₃¹⁹ have been extensively investigated.

Recently, BiCuSeO has received extensive attention, as a potential thermoelectric material with ZT value > 1 , achievable with elemental doping.^{20, 21} Owing to alternating layers of (Bi₂O₂)²⁺ and (Cu₂Se₂)²⁻, BiCuSeO exhibits natural superlattice structure, which results in an intrinsic low κ_t with tunable electrical properties.²² Furthermore, the natural superlattice has been found to significantly improve the Seebeck coefficient and decouple the thermal and electrical transportation of heat.²³ Several reports have discussed the partial substitution of Bi³⁺ with bivalent (Mg,²⁴ Pb,^{20, 25} Ca²⁶ and Sr^{27, 28}) or monovalent (K²⁹, Na³⁰) elements in order to optimize the carrier concentration and, thereby, higher ZT values of 0.7~1.1 have been achieved. Moreover, the highest ZT value of 1.4 in Ba-doped BiCuSeO respectively via grain-texturing³¹ and modulating doping³² has been obtained successfully.

Nevertheless, nearly all the bulk thermoelectric materials are synthesized by multi-step solid-state reactions,²⁶ melting followed by slow cooling,³³ and melting followed by annealing and mechanical alloying.³⁴ These processing routes are time- and energy-consuming, and to control the stoichiometry of volatile elements is yet another challenge. On the other hand, self-propagating high-temperature synthesis (SHS) is a synthesis route that accomplishes this typically on the timescale of seconds. A number of materials have been successfully synthesized by this method.³⁵⁻⁴⁰

Herein, we report the successful synthesis of BiCuSeO via SHS, and in order to confirm the compatibility of SHS method for doped BiCuSeO systems, Pb was doped

at Bi site, which has been reported as a promising dopant in BiCuSeO.²⁰ The Debye-Callaway model was employed in order to understand the thermal transport mechanism in pristine and Pb-doped BiCuSeO samples.

Experimental

Polycrystalline BiCuSeO was first prepared by meticulous mixing of Bi (99.99%, Aladdin), Bi₂O₃ (99.99%, Aladdin), PbO (99.9%, Aladdin), Cu (99.99%, Aladdin) and Se (99.99%, Aladdin). The obtained stoichiometric mixture was cold-pressed into pellets, which were brought to the ignition point using a torch flame. The obtained chunks were crushed and ground into fine powders, and then they were compacted to pellets having a diameter of 20mm by spark plasma sintering (SPS) at 973K for 5min under a uniaxial pressure of 50MPa.

The phase purity and crystal structure were investigated by X-ray diffraction (XRD, Bruker, Germany). The microstructure of the samples with different compositions and the samples obtained after hot corrosion were examined by field-emission scanning electron microscopy (SEM: LEO1530, Oxford, UK) and transmission electron microscope (TEM, JEOL2011, Japan). The chemical compositions of the samples were determined using inductively coupled plasma-atomic emission spectrometer (VISTA-MPX, VARIN, USA). The sintered pellets were cut into squares of 10×10 mm² and bar-shaped specimens of 3×3×12 mm³ along their radial direction. The rectangular bars were used for the simultaneous measurement of S and σ from room temperature to 873K by a ZEM-3 (ULVAC,

Japan). The carrier concentration (n) and mobility were determined by Hall measurement system (ResiTest 8300, Toyo Corporation, Japan). The thermal diffusivity (D) and the specific heat (C_P) were simultaneously measured along the thickness-direction of the square-shaped sample having thickness 1.0-1.5mm by using laser flash method (LFA-457, Netzsch, Germany) under a continuous Argon flow. The total thermal conductivity (κ_{total}) was calculated by the formula $\kappa=DC_P\rho$, where ρ is the mass density measured by the Archimedes principle. The residual offcuts were used to determine the elemental uniformity by electron probe micro-analyzer (EPMA JXA-8230, JEOL, Japan). The band gap was measured from the optical spectra recorded by spectrophotometer (Lambda 950, PerkinElmer, USA). The uncertainties in the Seebeck coefficient and the electrical conductivity were within 5% and 10%, respectively. The uncertainty in the thermal conductivity was estimated to be 7%~10% by considering the uncertainties in D , C_P and ρ . To determine the ignition temperature and required heating speed, the 15 mg cold-pressed mixed pellets were put in a power-compensation differential scanning calorimeter (DSC-Q2000, TA, USA), with N₂ gas flowing at a rate of 50 mL min⁻¹. BiCuSeO powder synthesized by SHS underwent cyclic thermal analysis, cycling 5 times under simultaneous thermogravimetry and differential thermal analysis (TG-DTA, Mettler Toledo Star System, USA), each cycle was from 323K to 973K with a heating rate of 20 Kmin⁻¹ and from 973K to 323K with a cooling rate of -20Kmin⁻¹. All processes were performed under Argon.

Results and Discussion

The samples prepared by the SHS method reacted quickly; they only required several seconds to react. The color of samples changed from black to red (inset on graph Fig.1a) as the reaction occurred. The size of sample is recorded in the supporting information (Fig.S1). As shown in Fig. 1a, no impurity peak was found in the SHS powder and the following sintered pellet; these peaks correspond with the single phase BiCuSeO structure according to PDF#45-0296. Moreover, in order to determine the ignition temperature and required heating rate, we compared the DSC curve of reaction process, which is shown in Fig. 1b.

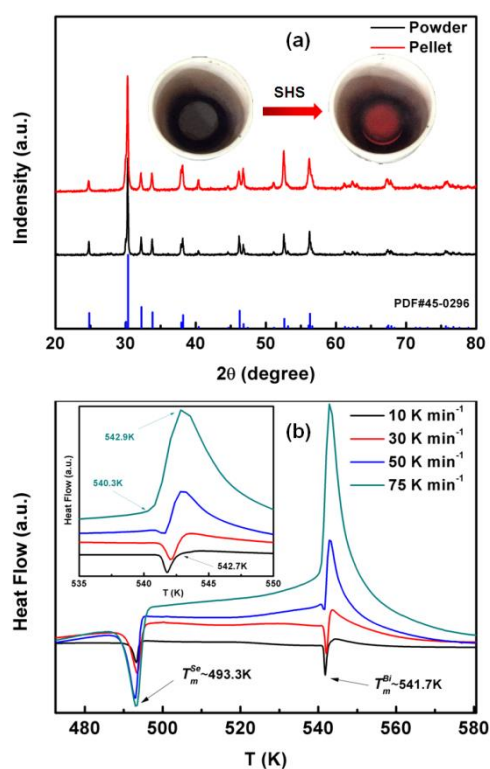


Fig. 1 (a) XRD patterns of pure BiCuSeO powder prepared by SHS and following SPSed pellet, the inset graph is the phenomenon of reaction. (b) DSC curves of reacting progress.

In traditional two-step solid state reaction, impurities still existed after 573K was reached with a heating rate set to 10 K min⁻¹. As shown in Fig. 1b, we selected heating rates of 10K min⁻¹, 30K min⁻¹, 50K min⁻¹ and 75K min⁻¹ as the constants for DSC, and for the first three process two endothermic peaks existed around 480K to 580K, corresponding to the melting point (T_m) of Se ($T_m \sim 493.3\text{K}$) and Bi ($T_m \sim 541.7\text{K}$) respectively, with no obvious exothermic peak between them. When the heating rate was increased to 75K min⁻¹, the second endothermic peak disappeared and the initial temperature of the much bigger and wider exothermic peak decreased from 542.7K to 540.3K, no other peaks were found in higher temperature regions (Fig.S2, supporting information), which indicate that SHS occurred and the ignition temperature is 540.7K. Combined with the binary or ternary alloys,³⁸ as there was no obvious exothermic peak between the two melting points for all heating rates process, the SHS process of BiCuSeO would have occurred when the temperature approached the second lowest melting point of the compound. The chemical reactions for SHS process are theorized to occur as follows:



Besides, the cyclic thermal analysis (Fig. S3, supporting information) suggests that the SHS powder does not have any phase transition and its weight loss is within the system's error range, which indicates that the powder reacts completely from 323K to 973K.

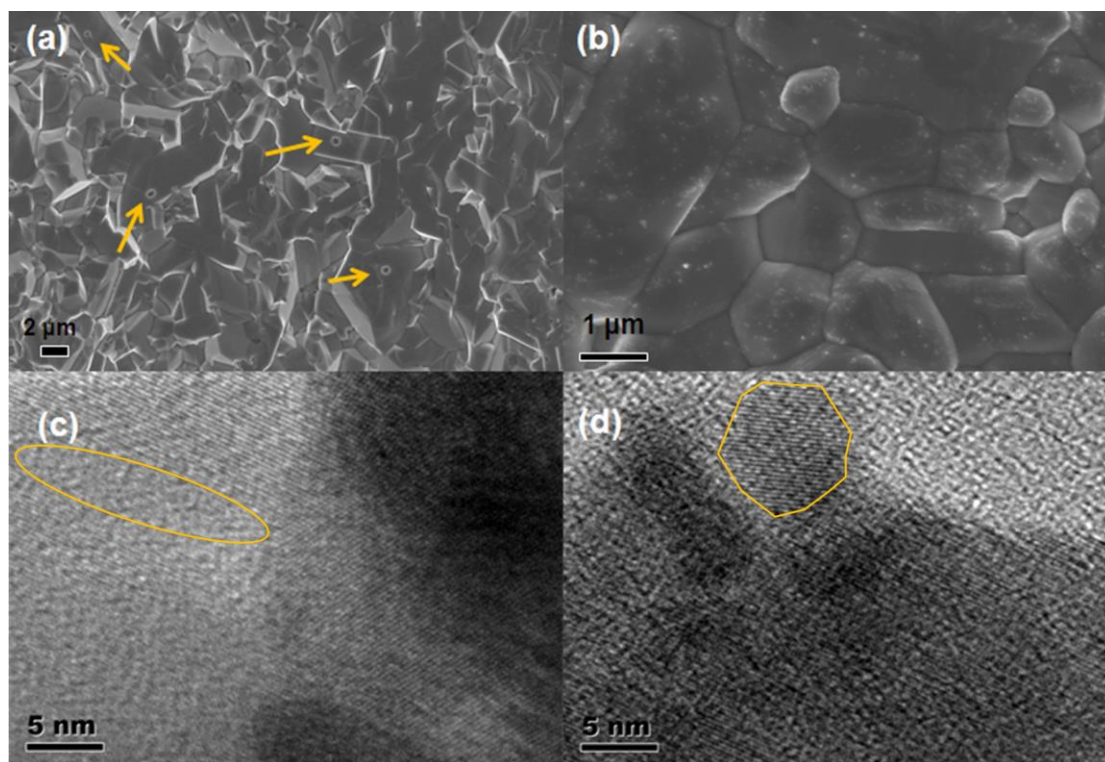


Fig. 2 (a) the microstructure of pure BiCuSeO synthesized by SHS-SPS with nano-pores indicated by yellow arrows, (b) grains after exposure to hot corrosion, (c) the amorphous region indicated by TEM, (d) 7-8nm nanoparticles exhibited in BiCuSeO.

The morphologies and the sizes of as-synthesized products were characterized by FESEM. As shown in Fig. 2a-b, the boundary compaction has been improved, which led to 97% relative density, and the grain size after SPS remained consistently 1-2 μ m, which was much bigger than 400-800 nm synthesized by SSR. The large grain size decreased boundary scattering for carriers, and further enhance electrical conductivity. There are ubiquitous nano-pores on the grain surfaces. These pores were possibly generated by the volatilization of surplus Se during the superfast reaction, which would enhance the scattering of mid- and long- wavelength phonons. It is well known that the SHS process would possibly introduce some new microstructure for materials,

just like nanostructure in Cu_2Se ,³⁸ a subtle observation of microstructure by TEM were shown in Fig. 2c-d, and the existence of an amorphous region and nanoparticles (~7-8nm) in BiCuSeO were proven. As the mean free paths of most phonons were close to several nanometers, we suspected these new regions would be the cause of the intrinsic low thermal conductivity.

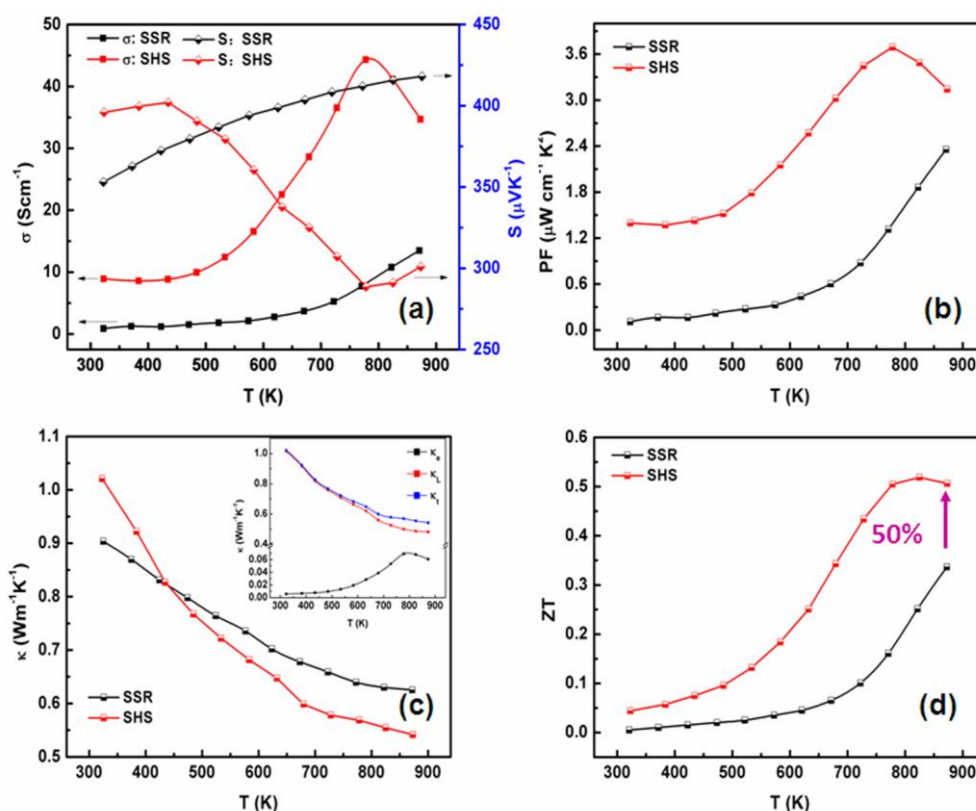


Fig. 3 Thermoelectric properties of BiCuSeO synthesized by SSR and SHS. (a) Temperature-dependent electrical conductivity and Seebeck coefficient, (b) power factor, (c) thermal conductivity, the inset graph including electronic and lattice thermal conductivities, (d) thermoelectric figure of merit. Note the 873K point: the SHS product exhibits a ZT that is 1.5 times larger than that of the SSR product.

The temperature dependence of thermoelectric properties of BiCuSeO synthesized by SSR³⁰ and SHS-SPS are presented in Fig. 3. It can be seen that the σ of

the samples prepared by SHS is much higher than that of the samples prepared by SSR, as shown in Figure 3a. This enhancement can be associated to the mentioned increased grain sizes and the improved grain alignment, which could come from the fact that SHS didn't give the grains enough time to form specific orientations like in SSR.⁴¹ As the difference of Seebeck coefficient between these two samples was not as large as the difference between σ , a higher power factor (PF) value of $3.2 \mu\text{W cm}^{-1} \text{K}^{-2}$ at 873K was obtained by SHS. Furthermore, the total thermal conductivity of the sample prepared by SHS was lower than that of sample prepared by SSR at high temperature, which can be expressed as a sum of the lattice thermal conductivity (κ_L) and the electronic thermal conductivity (κ_e) (see Fig.3c). κ_e can be estimated by Wiedemann-Franz law, as given below:

$$\kappa_e = L_0 \sigma T = ne \mu L_0 T, \quad (3)$$

where L_0 is the Lorentz number, which is estimated based on single band model and electron-phonon interaction (see Fig. S4, supporting information).

Based upon the enhanced power factor and the suppressed thermal conductivity, a relatively higher ZT value of 0.51 at 873K was obtained by SHS, which is tremendously (1.5 times) larger than that of the sample prepared by SSR. In order to optimize the thermoelectric performance of BiCuSeO, we combined SHS with the effect of Pb-doping.²⁰ XRD patterns of Pb-doped BiCuSeO are shown in Figure 4a, in which inset shows that the diffraction peaks have been shifted towards lower angle, owing to the larger ionic radius of Pb^{2+} (129pm) as compared to Bi^{3+} (117pm) (the coordination number is 8). This shift implies that Pb^{2+} has been substituted in the

lattice at Bi^{3+} site. The actual elemental compositions of the samples were determined by ICP-AES (shown in Table 1), combined with the elemental distribution obtained by EDS and EPMA, as shown in Fig. 4b-c, which indicated that the actual Pb contents in the samples were in good agreement with that of the theoretical calculated values and that the major elements were distributed homogeneously.

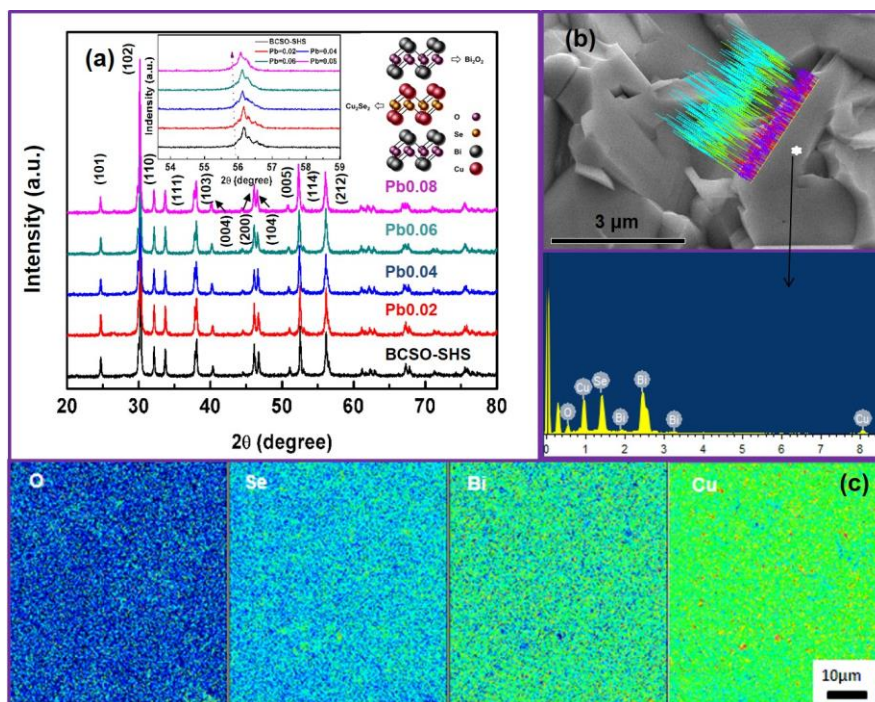


Fig. 4 (a) The XRD patterns of Pb-doped BiCuSeO, (b) line-scan and point analysis by EDS, (c) pure BiCuSeO: surface distribution of elements by EPMA.

Table 1: Chemical analysis by ICP-AES for $\text{Bi}_{1-x}\text{Pb}_x\text{CuSeO}$

| x | Bi | Cu | Se | Pb | Bi | Cu | Se | Pb |
|------------------|---------------|---------------|---------------|---------------|---------------|---------------|---------------|---------------|
| (Pb at %) | (wt %) |
| 0 | 54.84 | 18.36 | 17.33 | 0 | 1 | 1.101 | 0.836 | 0 |
| 0.02 | 54.34 | 18.40 | 19.02 | 1.08 | 0.980 | 1.092 | 0.908 | 0.020 |
| 0.04 | 48.93 | 18.22 | 18.48 | 2.04 | 0.960 | 1.175 | 0.959 | 0.040 |
| 0.06 | 50.82 | 18.21 | 19.66 | 3.24 | 0.940 | 1.107 | 0.962 | 0.060 |
| 0.08 | 51.08 | 18.14 | 18.2 | 4.24 | 0.923 | 1.078 | 0.870 | 0.077 |

Here, it should be noted that $\text{Bi}_{1-x}\text{Pb}_x\text{CuSeO}$ is degenerate compound as inferred from the electrical conductivity, shown in Fig. 5a. The electrical conductivity was dramatically enhanced from 9 Scm^{-1} ($x=0$) to 696 Scm^{-1} ($x=0.08$) at 323K through Pb doping, which is associated to the increased carrier concentration as described in Eq.

(4):



with more Pb^{2+} introduced to the lattice, the slope of the graph for electrical conductivity becomes smaller and the electrical transport behavior of Pb-doped BiCuSeO becomes more like that of metals rather than that of semiconductors. The temperature dependence of Seebeck coefficient for all the Pb-doped samples $\text{Bi}_{1-x}\text{Pb}_x\text{CuSeO}$ is shown in Fig. 5b. S decreases over the whole measured temperature range and there is a general trend that increasing Pb-doping level reduces S from $395 \mu\text{VK}^{-1}$ ($x=0$) to $106 \mu\text{VK}^{-1}$ ($x=0.08$) at 323K, which is consistent with the increasing carrier concentration as defined in Eq. (4), and shown in Fig. 6:

$$S = \frac{8\pi^2 k_B^2 T m^*}{3eh^2} \left(\frac{\pi}{3n}\right)^{2/3}, \quad (5)$$

where n is the carrier concentration, k_B is the Boltzmann constant and m^* is the effective mass of carrier. The expression in Eq. (5) is assumed for parabolic band and acoustic phonon scattering approximation, which can be applied for metals or degenerate semiconductors.

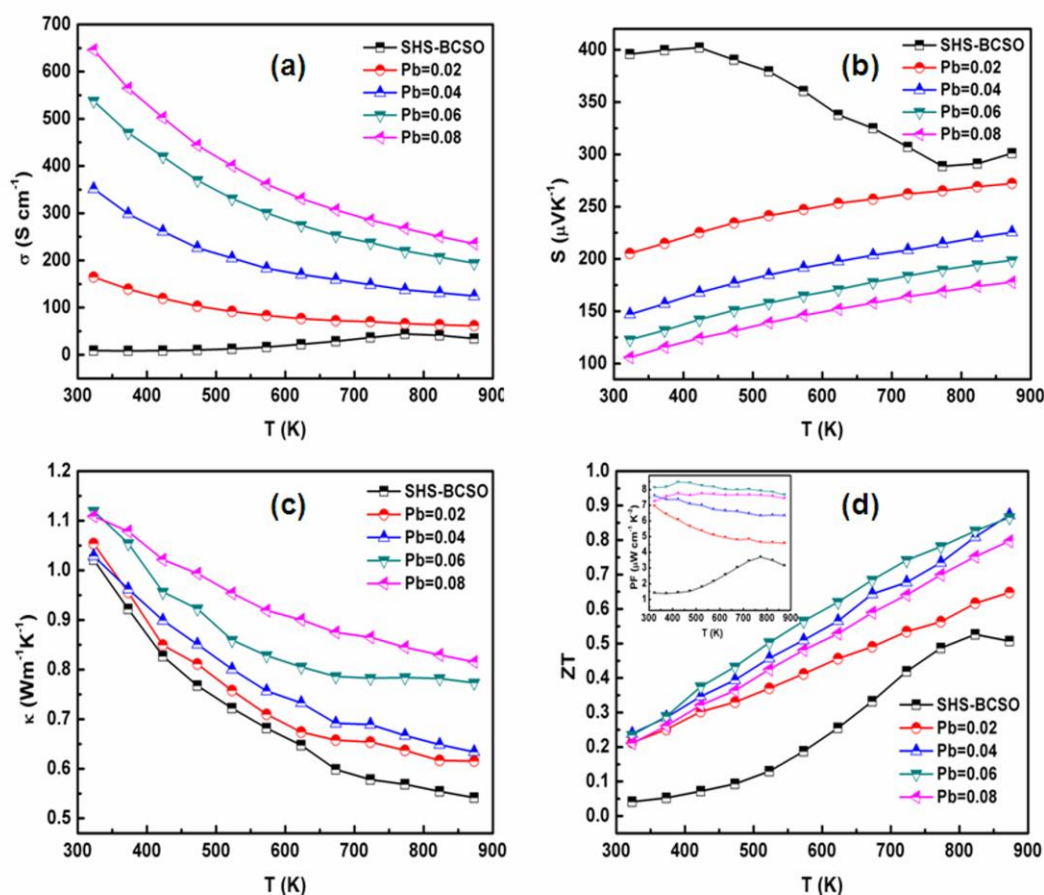


Fig. 5 The thermoelectric properties of Pb-doped BiCuSeO, temperature-dependent (a) electrical conductivity, (b) Seebeck coefficient, (c) thermal conductivity, (d) thermoelectric figure of merit, inset graph being power factor.

Hall Effect measurements were performed for the sake of analyzing the enhancement in the electrical transport properties, and m^* was calculated to investigate the actual carrier movements in BiCuSeO (Table 2). The indirect wide band gap in BiCuSeO was determined by infrared spectroscopy,⁴² as shown in Fig. 6a and Table 2. From the results of band gap determination, it can be seen that, with increasing Pb content, the band gap is narrowed. This is consistent with the increased carrier concentration and electrical conductivity. From Fig. 6b, we observed that the carrier concentration (n) increases markedly with an increased Pb-doping level and,

accordingly, the carrier mobility (μ) is decreased. However, one question that needs to be asked is this: Why do the different valances of Bi and Pb occupying the same lattice location lead to the change in the width of the band gap? We theorize it is related to the different valence band structures of Bi and Pb, which requires further investigation. Here, we assumed that all the Pb dopants have been substituted to Bi site and each Pb^{2+} ion introduces one hole as defined by Eq. (4). The experimentally determined n very nearly agrees with that of the calculated value. Based on the single band assumption (supporting information), we calculated m^* and estimated that our results were discrepant from that reported by *Lan et. al.*, which is possibly due to an effect of the microstructure.

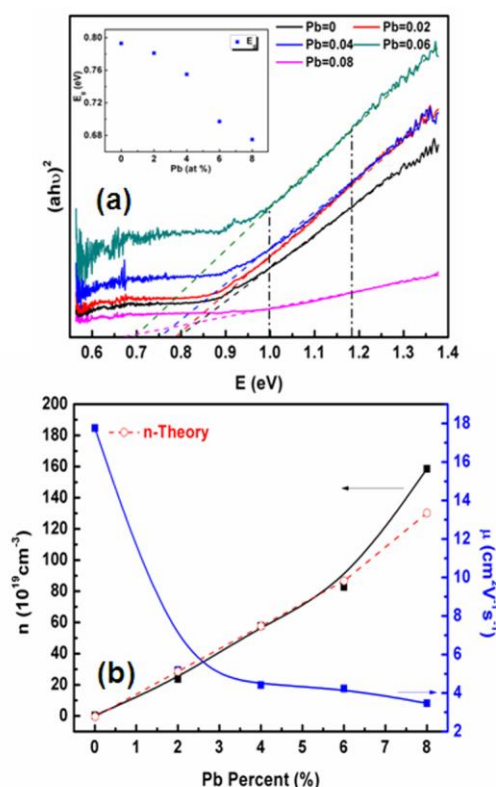


Fig. 6 (a) Energy gap of Pb-doped BiCuSeO measured by Infrared Spectroscopy, (The inset graph Pb percent-dependent E_g), (b) carrier concentration and mobility (The red

dotted line is the theoretical carrier concentration assumed by complete replacements).

The SHS method introduced a higher carrier concentration as compared to that of the SSR reaction after Pb doping. This enhancement is attributed to the refined grains and the discrepancy was broadened with the enlarged Pb content. However, the increasing m^* based on Pb-doping led to a decreased mobility for BiCuSeO. There are two contradictory opinions about the band effective mass m^* : a few reports have stated that a smaller m^* is better, whereas other reports suggested that a larger m^* is better for a higher Seebeck coefficient.⁴³⁻⁴⁵ As the Seebeck coefficient of BiCuSeO decreases quickly with Pb-doping, combining SHS with elemental doping to enlarge m^* on the premise of proper carrier mobility is a promising strategy to optimize its performance.

Table 2: The comparison of electrical transport properties of the samples synthesized by SSR-SPS²⁰ and SHS-SPS

| Pb (at %) | $n(\times 10^{19}\text{cm}^{-3})$ | | $\mu(\text{cm}^2\text{V}^{-1}\text{s}^{-1})$ | | $m^*(m_0)$ | | $E_g(\text{eV})$ |
|--------------|-----------------------------------|---------|--|---------|------------|---------|------------------|
| | SSR-SPS | SHS-SPS | SSR-SPS | SHS-SPS | SSR-SPS | SHS-SPS | SHS-SPS |
| 0 | 0.62 | 0.29 | 5.46 | 17.76 | 1.74 | 0.25 | 0.793 |
| 0.02 | | 23.66 | | 5.19 | | 6.46 | 0.781 |
| 0.04 | 25.0 | 57.82 | 5.32 | 4.42 | 5.39 | 7.36 | 0.755 |
| 0.06 | 34.1 | 82.73 | 7.46 | 4.24 | 4.84 | 6.86 | 0.697 |
| 0.08 | 86.6 | 158.58 | 3.96 | 3.47 | 4.76 | 9.07 | 0.675 |

The thermal conductivity of Pb-doped samples is shown in Fig. 5c and Fig. 7, both κ_t and κ_L decrease with increasing temperature, meanwhile the slope of κ_e varies only a little. *Yang et al.* suggested that the phonon scattering is induced by the boundary scattering at low temperatures, by the defect scattering at intermediate

temperatures, and by the Umklapp processes at high temperature.⁴⁶ It can be seen in Fig. 7 that the increased Pb content leads to a decreased κ_L near room temperature, and this advantage is reduced at high temperature because of the static Umklapp scattering which comes from the limitation of phonon-phonon scattering. For BiCuSeO, many researchers have reported an intrinsic low κ_L which approaches or is even below the glassy limit of thermal conductivity κ_{min} , as defined by Cahill's formulation.⁴⁷

$$\kappa_L = \frac{1}{2} \left(\frac{\pi}{6}\right)^{1/3} k_B V^{-2/3} (2v_t + v_l), \quad (6)$$

where V is the average volume per atom calculated from the refined lattice parameters, v_l , v_t are the longitudinal and transverse components of the speed of sound, respectively. Therefore the high temperature limit for the minimum lattice thermal conductivity approaches to a value of $\kappa_{min} = 0.59 \text{ Wm}^{-1}\text{K}^{-1}$. In the present work, we have obtained nano-pores, amorphous regions and nanoparticles over the grain of the samples, which may further decrease the lattice thermal conductivity κ_L , even below the glassy limit, as shown in Fig. 7. However, due to an increased electrical conductivity, κ_e has also been increased and for the 8% Pb-doped sample it reaches a value of $0.31 \text{ Wm}^{-1}\text{K}^{-1}$ at 873K, which results in a higher total thermal conductivity of $0.82 \text{ Wm}^{-1}\text{K}^{-1}$ for 8% Pb-doped sample at 873K. Consequently, improved electrical properties achieved by SHS method and Pb doping, combined with suppressed thermal conductivity determined by intrinsic properties and new microstructure, results in a higher ZT value of 0.91 at 873K for the 4% Pb-doped sample, as shown in Fig. 5d.

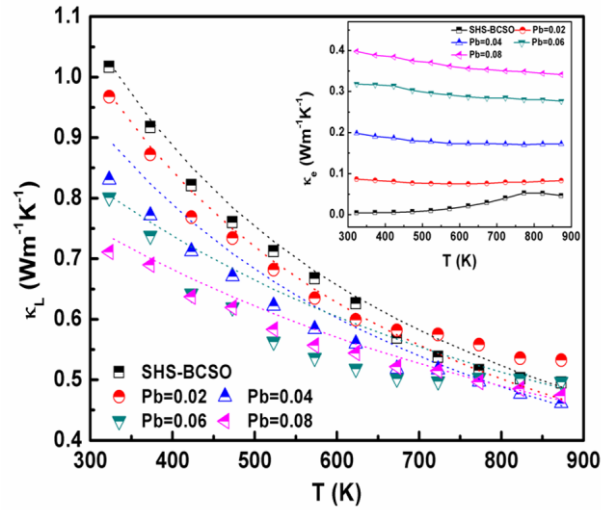


Fig. 7 Experimental lattice thermal conductivity (point) and the theoretical one calculated by Debye-Callaway model (dotted line), the inset graph being the electronic thermal conductivity based on Wiedemann-Franz law.

In order to understand the thermal transport mechanism in BiCuSeO, we fit the experimental data using the Debye-Callaway model, which can be written as;

$$\kappa_L = \frac{k_B}{2\pi^2\nu} \left(\frac{k_B}{h}\right)^3 T^3 \int_0^{\frac{\Theta_D}{T}} \frac{\tau_c x^4 e^x}{(e^x - 1)^2} dx, \quad (7)$$

where $x = h\omega/k_B T$ is a dimensionless quantity, ω the phonon frequency, h Planck's constant, Θ_D the Debye temperature, ν the velocity of sound and τ_c the relaxation time. The overall relaxation rate τ_c^{-1} can be determined by combining the various scattering processes as given:

$$\tau_c^{-1} = \tau_N^{-1} + \tau_b^{-1} + \tau_d^{-1} + \tau_U^{-1}, \quad (8)$$

where, τ_N , τ_b , τ_d and τ_U are the relaxation times for normal process scattering, boundary scattering, defect scattering and Umklapp scattering respectively, which are defined as:

$$\tau_b^{-1} = \nu/L, \quad (9)$$

$$\tau_d^{-1} = A\omega^4, \quad (10)$$

and

$$\tau_U^{-1} \sim \omega^\alpha (T / \Theta_D)^\beta \exp(-\Theta_D / bT), \quad (11)$$

L is the grain size for polycrystalline sample, and A is a constant which is independent of temperature and frequency. There is no satisfactory theoretical work for the relaxation time model to be used in Umklapp and normal processes. However, Slack reported an expression for the relaxation time to be used in Umklapp model as given in Eq. (11), in which, α , β , and b are constants.³⁴ In this work, we choose $\alpha=2$, $\beta=1$, and $b=2.4$, and the model had been successfully applied by Argawal and Verma.⁴⁸

By combining all the primary scattering parameters, we calculated κ_L to investigate the thermal transport mechanism in BiCuSeO. The results are shown in Fig. 7 (dotted line). Increased Pb dopants introduced increased mass and strain fluctuations, which play an important role in decreasing the thermal conductivity through enhanced defect scattering, especially at room temperature. Further, for BiCuSeO, Debye-Callaway model demonstrates that Umklapp scattering mechanism dominates in thermal transportation at high temperature. Nevertheless, the difference between the experimental data and the theoretical simulation is fairly distinct at 400-700K, especially for samples with 4% and 6% Pb. This implies that the Debye-Callaway model including normal process scattering, boundary scattering, defect scattering and Umklapp scattering still needs further optimization. It must be expanded to consider the contribution of nano-pores, amorphous regions and nanoparticles that were indicated by SEM and TEM.

Conclusions

SHS is a time- and energy-saving method for the synthesis of BiCuSeO oxyselenides. The ignition temperature of BiCuSeO oxyselenides is 540.3K, with a heating rate of 75Kmin⁻¹, which approaches the second lower melting point (Bi) of the compound. SHS simultaneously enhanced the electrical conductivity and suppressed lattice thermal conductivity for BiCuSeO with refined grain size, equally distributed nano-pores, amorphous regions and nanoparticles. After substituting Pb²⁺ for Bi³⁺, the energy gap (E_g) was narrowed and the effective mass (m^*) was increased with increasing doping level, which was responsible for the enhanced power factor. Furthermore, the lattice thermal conductivity (κ_L) data could be reproduced by the Debye-Callaway model, which reveals that the main contribution in κ_L at room temperature associated to the induced point defects by Pb-doping. Finally, for Bi_{1-x}Pb_xCuSeO a ZT value of up to 0.91 at 873K could be reached in the 4% Pb-doped sample. By combining the ultrafast SHS method with the other promising strategies followed for improving the thermoelectric performance, BiCuSeO can make an efficient p-type candidate for commercial applications.

Acknowledgements

We thank Professor Jingfeng Li and Doctor Qing Tan from Tsinghua University for accurate characterization, also thank Doctor Huaizhou Zhao and Doctor Shanming Li from Institute of Physics, Chinese Academy of Science for valuable discussions. This work was financially supported by the Ministry of Sci. & Tech. of China through

a 973-Project, under grant No. 2013CB632506, NSF of China under Grant No. 51202232 and 11234012, and Specialized Research Fund for the Doctoral Program of Higher Education, under grant No.20120002110006.

Notes and references

1. J. P. Heremans, V. Jovovic, E. S. Toberer, A. Saramat, K. Kurosaki, A. Charoenphakdee, S. Yamanaka and G. J. Snyder, *Science*, 2008, 321, 554-557.
2. D. M. Rowe, *Thermoelectrics handbook: macro to nano*, CRC press, 2005.
3. J. S. Rhyee, K. H. Lee, S. M. Lee, E. Cho, S. I. Kim, E. Lee, Y. S. Kwon, J. H. Shim and G. Kotliar, *Nature*, 2009, 459, 965-968.
4. M. S. Dresselhaus, G. Chen, M. Y. Tang, R. Yang, H. Lee, D. Wang, Z. Ren, J. P. Fleurial and P. Gogna, *Adv. Mater.*, 2007, 19, 1043-1053.
5. G. Chen, M. Dresselhaus, G. Dresselhaus, J.-P. Fleurial and T. Caillat, *Int. Mater. Rev.*, 2003, 48, 45-66.
6. T. Tritt, *Advances in Thermoelectric Materials I*, Academic Press, 2000.
7. G. S. Nolas, J. Poon and M. Kanatzidis, *MRS bull.*, 2006, 31, 199-205.
8. S. M. Kauzlarich, S. R. Brown and G. J. Snyder, *Dalton T.*, 2007, 2099-2107.
9. X. Tang, W. Xie, H. Li, W. Zhao, Q. Zhang and M. Niino, *Appl. Phys. Lett.*, 2007, 90, 012102-012103.
10. G. J. Snyder, *Energ. Environ. Sci.*, 2011, 4, 2085-2089.
11. X. Wang, H. Lee, Y. Lan, G. Zhu, G. Joshi, D. Wang, J. Yang, A. Muto, M. Tang and J. Klatsky, *Appl. Phys. Lett.*, 2008, 93, 193121-193121-193123.
12. S. Bhattacharya, A. L. Pope, R. T. Littleton, T. M. Tritt, V. Ponnambalam, Y. Xia and S. J. Poon, *Appl. Phys. Lett.*, 2000, 77.
13. Singh, D. J.; Mazin, I. I. *Phys. Rev. B* 1997, 56, R1650.
14. G. Xu, R. Funahashi, M. Shikano, I. Matsubara and Y. Zhou, *Appl. Phys. Lett.*,

2002, 80, 3760.

15. K. Fujita, T. Mochida and K. Nakamura, *Jpn. J. Appl. Phys.*, 2001, 40, 4644.

16. S.-M. Choi, C.-H. Lim and W.-S. Seo, *J. Elec. Mater.*, 2010, 40, 551-556.

17. J. Liu, C. L. Wang, H. Peng, W. B. Su, H. C. Wang, J. C. Li, J. L. Zhang and L. M. Mei, *J. Elec. Mater.*, 2012, 41, 3073-3076.

18. P. Jood, R. J. Mehta, Y. Zhang, G. Peleckis, X. Wang, R. W. Siegel, T. Borca-Tasciuc, S. X. Dou and G. Ramanath, *Nano lett.*, 2011, 11, 4337-4342.

19. Y. Liu, Y. H. Lin, J. Lan, W. Xu, B. P. Zhang, C. W. Nan and H. Zhu, *J. Am. Ceram. Soc.*, 2010, 93, 2938-2941.

20. J. L. Lan, Y. C. Liu, B. Zhan, Y. H. Lin, B. Zhang, X. Yuan, W. Zhang, W. Xu and C. W. Nan, *Adv. Mater.*, 2013, 25, 5086-5090.

21. F. Li, J.-F. Li, L.-D. Zhao, K. Xiang, Y. Liu, B.-P. Zhang, Y.-H. Lin, C.-W. Nan and H.-M. Zhu, *Energ. Environ. Sci.*, 2012, 5, 7188-7195.

22. J. Li, J. Sui, Y. Pei, C. Barreateau, D. Berardan, N. Dragoe, W. Cai, J. He and L.-D. Zhao, *Energ. Environ. Sci.*, 2012, 5, 8543-8547.

23. Y. Liu, L.-D. Zhao, Y. Liu, J. Lan, W. Xu, F. Li, B.-P. Zhang, D. Berardan, N. Dragoe and Y.-H. Lin, *J. Am. Chem. Soc.*, 2011, 133, 20112-20115.

24. J. L. Lan, B. Zhan, Y. C. Liu, B. Zheng, Y. Liu, Y.-H. Lin and C. W. Nan, *Appl. Phys. Lett.*, 2013, 102, 123905.

25. L. Pan, D. B éardan, L. Zhao, C. Barreateau and N. Dragoe, *Appl. Phys. Lett.*, 2013, 102, 023902.

26. Y.-L. Pei, J. He, J.-F. Li, F. Li, Q. Liu, W. Pan, C. Barreateau, D. Berardan, N.

- Dragoe and L.-D. Zhao, *NPG Asia Mater.*, 2013, 5, e47.
27. L. Zhao, D. Berardan, Y. Pei, C. Byl, L. Pinsard-Gaudart and N. Dragoe, *Appl. Phys. Lett.*, 2010, 97, 092118-092118-092113.
28. C. I. Barreteau, D. Bérardan, E. Amzallag, L. Zhao and N. Dragoe, *Chem. Mater.*, 2012, 24, 3168-3178.
29. D. Sun Lee, T.-H. An, M. Jeong, H.-S. Choi, Y. Soo Lim, W.-S. Seo, C.-H. Park, C. Park and H.-H. Park, *Appl. Phys. Lett.*, 2013, 103, 232110.
30. J. Li, J. Sui, Y. Pei, X. Meng, D. Berardan, N. Dragoe, W. Cai and L.-D. Zhao, *J. Mater. Chem. A*, 2014, 2, 4903-4906.
31. J. Sui, J. Li, J. He, Y.-L. Pei, D. Berardan, H. Wu, N. Dragoe, W. Cai and L.-D. Zhao, *Energy Environ. Sci.*, 2013, 6, 2916-2920.
32. Y. L. Pei, H. Wu, D. Wu, F. Zheng and J. He, *J. Am. Chem. Soc.*, 2014.
33. K. F. Hsu, S. Loo, F. Guo, W. Chen, J. S. Dyck, C. Uher, T. Hogan, E. Polychroniadis and M. G. Kanatzidis, *Science*, 2004, 303, 818-821.
34. D. Morelli, T. Caillat, J.-P. Fleurial, A. Borshchevsky, J. Vandersande, B. Chen and C. Uher, *Phys. Rev. B*, 1995, 51, 9622.
35. A. G. Merzhanov, *Combustion and plasma synthesis of high-temperature materials*, 1990, 1-53.
36. J. Kingsley and K. Patil, in *Ceramic powder science* 3, 1990.
37. H. Yi and J. Moore, *J. Mater. Sci.*, 1990, 25, 1159-1168.
38. X. Su, F. Fu, Y. Yan, G. Zheng, T. Liang, Q. Zhang, X. Cheng, D. Yang, H. Chi and X. Tang, *Nat. Commun.*, 2014, 5.

39. F. Rouessac and R.-M. Ayrat, *J. Alloy. Compd.*, 2012, 530, 56-62.
40. J. Selig, S. Lin, H.-T. Lin and D. Johnson, *J. Aust. Ceram. Soc.*, 2012, 48.
41. G. K. Ren, S. Butt, Y. C. Liu, J. L. Lan, Y. H. Lin, C. W. Nan, F. Fu and X. F. Tang, *Phys. status solidi (a)*, 2014.
42. S. Butt, N. A. Shah, A. Nazir, Z. Ali and A. Maqsood, *J. Alloy. Compd.*, 2014, 587, 582-587.
43. Y. Pei, X. Shi, A. LaLonde, H. Wang, L. Chen and G. J. Snyder, *Nature*, 2011, 473, 66-69.
44. G. J. Snyder and E. S. Toberer, *Nat. Mater.*, 2008, 7, 105-114.
45. Y. Pei, H. Wang and G. J. Snyder, *Adv. Mater.*, 2012, 24, 6125-6135.
46. J. Yang, G. P. Meisner, D. T. Morelli, C. Uher, *Phys. Rev. B*, 2000, 63, 014410.
47. K. S. Weldert, W. G. Zeier, T. W. Day, M. Panthofer, G. J. Snyder and W. Tremel, *J. Am. Chem. Soc.*, 2014, 136, 12035-12040.
48. B. K. Agrawal and G. Verma, *Phys. Rev.*, 1962, 128, 603.